Nano Energy 92 (2022) 106762

Contents lists available at ScienceDirect

Nano Energy

journal homepage: www.elsevier.com/locate/nanoen

Theoretical model and optimal output of a cylindrical triboelectric nanogenerator

Xin Guo [a,b,1], Jiajia Shao [a,1], Morten Willatzen [a,b], Yi Yang [c], Zhong Lin Wang [a,b,d,e,*]

[a] Beijing Institute of Nanoenergy and Nanosystems, Chinese Academy of Sciences, Beijing 101400, PR China
[b] School of Nanoscience and Technology, University of Chinese Academy of Sciences, Beijing 100049, PR China
[c] Research Laboratory of Electronics, Massachusetts Institute of Technology, Cambridge, MA, United States
[d] CUSTech Institute, Wenzhou, Zhejiang 325024, PR China
[e] School of Materials Science and Engineering, Georgia Institute of Technology, Atlanta, GA 30332-0245, United States

ARTICLE INFO

Keywords:
Cylindrical triboelectric nanogenerator
Energy output efficiency
Three-dimensional cylindrical mathematical model
Expanded Maxwell's equations
Maxwell's displacement current

ABSTRACT

Conversion of mechanical energy into electricity using triboelectric nanogenerators is at the forefront of alternative energy technology. However, the advancement of accurate modeling of cylindrical TENG energy harvesting process is proceeding slowly. Previous theoretical models are built based on charged finite-sized planes which cannot be applied to more general situations where charges are distributed in complex geometric configurations. Such models are inaccurate and inadequate to describe field phenomena on a larger spatial scale. Here, a systematic theoretical analysis of a three-dimensional cylindrical triboelectric nanogenerator is presented based on expanded Maxwell's equations which establishes a standard framework for modeling non-planar elementary geometric structures such as cones, arcs, disks, etc. Most importantly, the time- and spatial-dependent electric field and electric displacement produced by the cylindrical distribution of charges are fully unveiled, clarifying how the energy conversion mechanism is using Maxwell's displacement current as well as allowing quantitative analyses of the power dynamics, energy output efficiency, and basic output characteristics of the cylindrical triboelectric nanogenerator. The model analysis presented in this work is helpful to improve the fundamental theory of triboelectric nanogenerators and allows constructing complex mechanical energy harvesting systems conforming accurately and more realistically to practical situations.

1. Introduction

Effectively converting the widely distributed and disorganized mechanical energy into electricity with triboelectric nanogenerators (TENGs) is receiving extensive and increasing attention [1–5]. A typical TENG device consists of at least two parts, the dielectric media which generates the electrostatic charges, and the electrodes that response to the induced charges [6–9]. When the electrodes are connected, a displacement current is generated inside the TENG device and a conduction current flows through the external circuit, and the two different currents are jointed together forming a closed loop [10–14]. Although a multitude of TENGs with different configurations have been fabricated as energy harvesters/self-powered sensors [15–17], these consistent reports are generally observational, making it difficult to fully comprehend the relevant working mechanism, especially for the case of a complex, dynamic charge distribution. This is mainly because a detailed theoretical model has not been developed hitherto.

Establishing a 3D theoretical model of a TENG device allows a detailed understanding of the charge distribution. Till now although some models have been presented, they are built based on a series of finite-sized charged parallel plates, which can be utilized to investigate the TENGs with simple geometric structures [18–23]. But these theoretical models are inadequate to represent complex geometric configurations such as arcs, cones, cylinders, etc. A distance-dependent electric field (DDEF) model has been proposed by Dharmsena et al., which can be utilized to describe convex and concave charged surfaces, but except for exploring the outputs of the lateral sliding mode TENG; since there is no appropriate coordinate system in this model [22]. Accordingly, they cannot be extended to determine the time-varying electric field and electric potential of TENGs that appear quite frequently in practical

* Corresponding author at: Beijing Institute of Nanoenergy and Nanosystems, Chinese Academy of Sciences, Beijing 101400, PR China.
E-mail address: zlwang@gatech.edu (Z.L. Wang).
[1] These authors contributed equally to this work.

https://doi.org/10.1016/j.nanoen.2021.106762
Received 26 September 2021; Received in revised form 29 October 2021; Accepted 14 November 2021
Available online 20 November 2021

applications [24,25]. In addition, essentially, there are two different quantities in an electromagnetic model: source quantities and field quantities. The charges which are stationary or in motion are traditionally regarded as the source of an electromagnetic field. We have proved that the quasi-electrostatic field distribution of TENG device may cause a redistribution of charges (in contacting surfaces and electrodes), which will, in turn, change the field under a continuously mechanical agitation [26,27]. Hence identifying the cause and the effect with clarity remains challenging, which significantly adds another layer of difficulty to build a general universal model for TENGs.

Here, through a combination of expanded Maxwell's equations and geometric construction, we propose a new cylindrical mathematical model for TENGs, by which the time-varying electric field, polarization, and electric displacement are comprehensively derived. The correctness and effectiveness of the theoretical model are demonstrated by FEM simulation and semi-analytical analysis, laying the foundation for modeling other more complex geometric structures with non-planar charge distributions. We confirm that the creation of a satisfactory mathematical model depends sensitively on the charge distributions in TENG devices, an aspect that has not received enough attention in the past. A capacitor model of the cylindrical mode TENG is also present, for the sake of comparison and utilization in different applications. The dynamic outputs such as effective transferred charge, voltage, average power, in particular the energy output efficiency is simulated at different mechanical conditions. Our results indicate that maintaining the TENG to operate at an optimum load resistance continuously, the root-mean-square transferred charge, voltage and the largest output efficiency (close to 70%) do not change as the mechanical frequency increases/decreases. We anticipate that the present quantitative analysis of the cylindrical model TENG allows to predict the output performance of TENGs with a complex spatial charge distribution significantly better than hitherto.

2. Results

2.1. Expanded Maxwell's equations

It has been proven that nanogenerators based on effects of triboelectric, piezoelectric, electrostatic, and/or electret are important research fields that use displacement current as the driving force [10,11]. Through Wang's addition of another source term–Wang term $\boldsymbol{P}_S$, the displacement current and Maxwell's equations are expanded, so that the underlying mechanism of nanogenerators can be thoroughly revealed [10,11,24]. As an example, when a dielectric material is placed in an external electric field, a lot of little dipole moments are induced and each dipole tends to point in the same direction as the field. The material becomes polarized, and its polarization is represented by $\boldsymbol{P}$. For such polarized dielectric media, Gauss's law changes to $\nabla \bullet \boldsymbol{D} = \sigma_f$, where σ_f is the free charges and $\boldsymbol{D}$ is known as the electric displacement, which reads $\varepsilon_0 \boldsymbol{E} + \boldsymbol{P}$. Note that here the term $\boldsymbol{E}$ represents the total electric field within the dielectric material. Remove the external electric field, the electric displacement $\boldsymbol{D}$ goes to zero (except for some special dielectrics such as the electret material). However, this is different from what happens during the TENG operation. In the case of TENG device, tribo-charges are generated on the contacting surfaces due to contact electrification under mechanical triggering. In order to identify the contribution from the surface charges that are independent of the external electric field, the Wang term $\boldsymbol{P}_S$ is added in electric displacement $\boldsymbol{D}$ [10,11],

$$\boldsymbol{D} = \varepsilon_0 \boldsymbol{E} + \boldsymbol{P} + \boldsymbol{P}_S \tag{1}$$

Note that in polarized dielectric media, the $\boldsymbol{D}$ may differ from the $\boldsymbol{E}$ since it is not necessarily irrotational; and it will have curl when the polarization does. The total displacement current density ($\boldsymbol{J}_D$) is:

$$\boldsymbol{J}_D = \frac{\partial \boldsymbol{D}}{\partial t} = \varepsilon_0 \frac{\partial \boldsymbol{E}}{\partial t} + \frac{\partial \boldsymbol{P}}{\partial t} + \frac{\partial \boldsymbol{P}_S}{\partial t} \tag{2}$$

The first term on the right side of Eq. (2) represents the time-varying electric field, through which the applicability of Ampere's law is extended to time-dependent conditions by Maxwell, and the term $\partial \boldsymbol{P}_S/\partial t$ is the polarization current density within dielectric media because any movement of charge constitutes an electric current; importantly the third term represents the displacement current due to the time rate of change of the external strain field, which has responsibility for the energy conversation [10,11,13,26]. This is the physical essence why the I_D is the internal driving force of TENGs. On the other hand, it is a starting point that we can utilize a coordinate system reflecting the geometry of TENG device to reveal the field quantities.

By a surface integral of $\boldsymbol{J}_D$, the displacement current (I_D) can be obtained:

$$I_D = \int_S \boldsymbol{J}_D \bullet d\boldsymbol{S} = \int_S \frac{\partial \boldsymbol{D}}{\partial t} \bullet \boldsymbol{n} \mathrm{d}\boldsymbol{S} = \frac{\partial}{\partial t} \int \nabla \bullet \boldsymbol{D} \mathrm{d}\boldsymbol{r} = \frac{\partial}{\partial t} \int \sigma_f \mathrm{dr} = \frac{\partial Q}{\partial t} \tag{3}$$

where Q represents the transferred charges (free charges) between the two electrodes of TENGs. It is worth noting that this equation connects the internal circuit and external circuit together, eventually forming a complete integration solution. Afterwards, through applying Coulomb's law for charge distributions, the electric potentials of each electrode (denoted by ϕ_A and ϕ_B, respectively) can be derived. When the external circuit is connected with a resistor Z, according to Kirchhoff's law and Ohm's law, the potential drop (ϕ_{BA}) across Z reads

$$\Phi_B - \Phi_A = \Phi_{BA} = -Z \frac{\partial Q}{\partial t} \tag{4}$$

In general, Eq. (4) is a first order ordinary differential equation depending on the external circuit conditions. Once the governing equation is solved, the output variables describing the dynamic performance of TENGs are determined. Essentially, this framework is linked by the fundamental laws of physics logically, which is expected to be applied to all the energy harvesting system based on nanogenerators.

It is well known that electromagnetic fields are generally functions of time and of space coordinates and represented by their magnitude and, for vector fields additionally, direction. Although the laws of electromagnetism are the same in all coordinate systems, relationships among variables are conveniently expressed in a coordinate system reflecting the geometry. This is the essential reason for using e.g. a rectangular or cylindrical coordinate representation for TENGs. It is important to realize; however, we still cannot fully predict all details in the input-output behavior of TENGs due to the sometimes unpredictable changes in the external circuit. The starting point for an analysis is Kirchhoff's law and the establishment of a time-dependent differential equation for the system and external circuit using a 3D description of the electromagnetic fields.

2.2. Mathematic model of the cylindrical LS mode TENG

Firstly, assume we have an arbitrary number of cylindrical sheets, all of the same length L, and their axis coincides with the z-axis. These cylindrical shells $i^1, i^2, \ldots, i^N$ are located at positions $z_1, z_2, \ldots, z_N$, with surface charge density $\sigma_1, \sigma_2, \ldots, \sigma_N$, and radius $R_1, R_2, \ldots, R_N$, respectively. The electric potential produced by these cylindrical charge distributions at an arbitrary observation point $\boldsymbol{p}$ (r, φ, z) is (Note S1, Supporting Information)

$$\Phi(r, \varphi, z) = \sum_{i=1}^{N} \int_0^{2\pi} \int_{z_i}^{z_i+L_i} \frac{\sigma_i R_i d\theta dz'}{4\pi\varepsilon(\boldsymbol{p})\sqrt{r^2 + R_i^2 - 2rR_i\cos(\varphi - \theta) + (z - z')^2}} \tag{5}$$

The corresponding radial (E_r (r, φ, z)) and axial (E_z (r, φ, z)) components of the electric field are:

$$E_r(r,\varphi,z)=\sum_{i=1}^{N}\int_0^{2\pi}\int_{z_i}^{z_i+L_i}\frac{\sigma_i R_i[r-R_i\cos(\varphi-\theta)]}{4\pi\varepsilon(\boldsymbol{p})\left[r^2+R_i^2-2rR_i\cos(\varphi-\theta)+(z-z')^2\right]^{\frac{3}{2}}}d\theta dz' \tag{6}$$

$$E_z(r,\varphi,z)=\sum_{i=1}^{N}\int_0^{2\pi}\int_{z_i}^{z_i+L_i}\frac{\sigma_i R_i(z-z')}{4\pi\varepsilon(\boldsymbol{p})\left[r^2+R_i^2-2rR_i\cos(\varphi-\theta)+(z-z')^2\right]^{\frac{3}{2}}}d\theta dz' \tag{7}$$

These above expressions allow us to construct a mathematical model for the cylindrical lateral sliding (LS) mode TENG in cylindrical coordinates.

A typical cylindrical LS mode TENG (Fig. 1b) consists of two parts: the sliding part and the fixed part which are comprised of dielectric media and metal electrodes (Fig. 1c). As the inner cylindrical shell (sliding part) moves up and down in the outer cylindrical shell (fixed part), charges are created and distributed on the contacting surfaces. We assume one contacting surface is charged uniformly positively while the other is charged uniformly negatively, and the triboelectric charge density remains constant when the TENG is in steady-state. It should be noticed that although previous examinations of contact electrification support a random "mosaic" of oppositely charged regions nanoscopic dimensions, the full effects of contact charging trends are considered in this work [28]. Indeed, the earlier simplifying assumption is exceedingly paramount [7,13,22,29]. From the viewpoint of classical electrodynamics, understanding the charge distribution and its variations is the foundation of establishing mathematical models for TENGs. Although electric charges move from one electrode to another and redistribute during TENG operation, the total number of positive and negative charges in the system must be equal. In other words, the rate of change of charge is zero at all times such that lump circuit abstraction theory can be applied to TENGs.

Generally, there are three operation cases of TENGs: open-circuit (OC) condition, short-circuit (SC) condition and loading condition, corresponding to different charge distributions. Under OC conditions, no charges are transferred between the two electrodes, consequently only tribo-charges are distributed on the contacting surfaces. At SC conditions, free charges flow in the external circuit to reduce the potential difference, leading to a more complex charge distribution. When a load resistance is used the charge transfer rate is reduced in comparison to SC

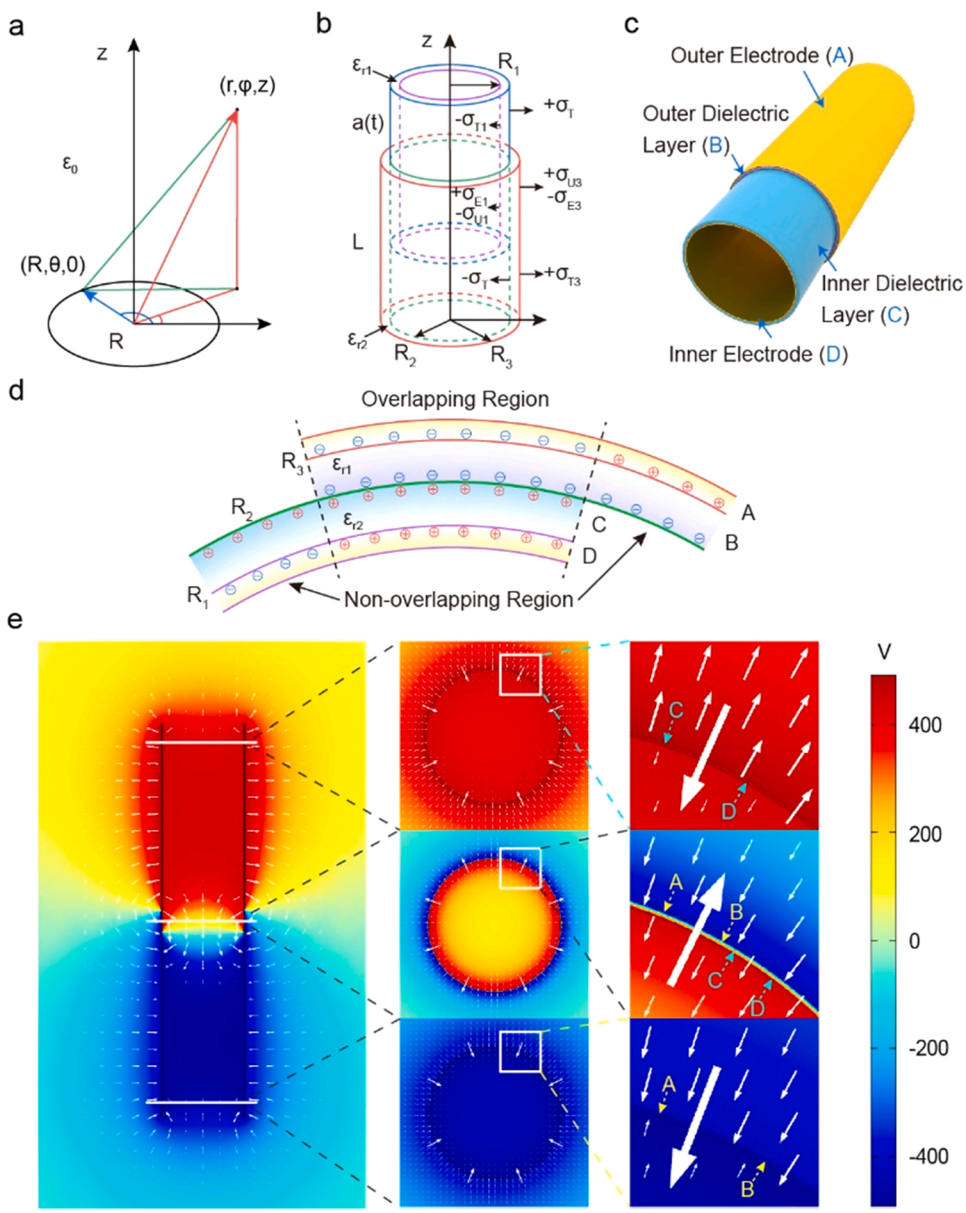

Fig. 1. Schematic of a cylindrical lateral sliding (LS) mode TENG in the cylindrical coordinate system, and finite element modeling (FEM) simulation at open-circuit (OC) conditions. (a) Schematic of a uniformly charged circular conductor and (b) a cylindrical LS mode TENG in cylindrical coordinates. (c) Structure of the cylindrical LS mode TENG. (d) Charge distributions at OC conditions. (e) Distribution of the electric potential (colors) and electric field (arrows) at OC condition when the relative moving distance $z = 0.9\ L$. Here L represents the length of TENG device.

conditions. For instance, there are six different charge distribution regions in the cylindrical mode TENG device denoted by (Note S2, Supporting Information):

On the non-overlapping region of the outer surface of the dielectric 1:σ_T;

On the non-overlapping region of the inner surface of the dielectric 2:-σ_T;

On the non-overlapping region of the inner electrode: $\sigma_{T1} = -\sigma_T\frac{R_2}{R_1}$;.

On the non-overlapping region of the external electrode: $\sigma_{T3} = \sigma_T\frac{R_2}{R_3}$;.

On the overlapping region of the inner electrode: $\sigma_{E1} = \sigma_T\frac{R_2 a(t)}{R_1(L-a(t))}$;.

On the overlapping region of the external electrode: $\sigma_{E3} = -\sigma_T\frac{R_2 a(t)}{R_3(L-a(t))}$;.

Transferred charges on the overlapping region of the inner electrode:-σ_{U1};

Transferred charges on the overlapping region of the external electrode:+σ_{U3};

By applying Coulomb's law and consideration of the azimuthal symmetry of the charge distribution (Fig. 1b), the electric potential ϕ (r, 0, z) of the cylindrical model TENG is (Note S2, Supporting Information):

$$\begin{aligned}
\Phi(r,0,z) &= +\frac{\sigma_T R_{2^-}}{4\pi\varepsilon}\int_0^{2\pi}\int_L^{L+a(t)}\frac{d\theta dz'}{\left[R_{2^-}^2+r^2-2rR_{2^-}\cos\theta+(z-z')^2\right]^{\frac{1}{2}}} \\
&-\frac{\sigma_T R_{2^+}}{4\pi\varepsilon}\int_0^{2\pi}\int_0^{a(t)}\frac{d\theta dz'}{\left[R_{2^+}^2+r^2-2rR_{2^+}\cos\theta+(z-z')^2\right]^{\frac{1}{2}}} \\
&+\frac{\sigma_{E1} R_1}{4\pi\varepsilon}\int_0^{2\pi}\int_{a(t)}^{L}\frac{d\theta dz'}{\left[R_1^2+r^2-2rR_1\cos\theta+(z-z')^2\right]^{\frac{1}{2}}} \\
&-\frac{\sigma_{T1} R_1}{4\pi\varepsilon}\int_0^{2\pi}\int_L^{L+a(t)}\frac{d\theta dz'}{\left[R_1^2+r^2-2rR_1\cos\theta+(z-z')^2\right]^{\frac{1}{2}}} \\
&+\frac{\sigma_{T3} R_3}{4\pi\varepsilon}\int_0^{2\pi}\int_0^{a(t)}\frac{d\theta dz'}{\left[R_3^2+r^2-2rR_3\cos\theta+(z-z')^2\right]^{\frac{1}{2}}} \\
&-\frac{\sigma_{E3} R_3}{4\pi\varepsilon}\int_0^{2\pi}\int_{a(t)}^{L}\frac{d\theta dz'}{\left[R_3^2+r^2-2rR_3\cos\theta+(z-z')^2\right]^{\frac{1}{2}}} \\
&+\frac{\sigma_{U3} R_3}{4\pi\varepsilon}\int_0^{2\pi}\int_{a(t)}^{L}\frac{d\theta dz'}{\left[R_3^2+r^2-2rR_3\cos\theta+(z-z')^2\right]^{\frac{1}{2}}} \\
&-\frac{\sigma_{U1} R_1}{4\pi\varepsilon}\int_0^{2\pi}\int_{a(t)}^{L}\frac{d\theta dz'}{\left[R_1^2+r^2-2rR_1\cos\theta+(z-z')^2\right]^{\frac{1}{2}}}
\end{aligned} \tag{8}$$

Here, σ_T, σ_E and σ_U represent the density of triboelectric charge, induced charge and transferred charge, respectively; L is the length of the cylindrical shell/electrode and a(t) is the axial separation distance; the radius of the inner surface of the internal dielectric cylindrical shell, the contacting surface and the outer surface of the external dielectric cylindrical shell are denoted R_1, R_2 and R_3, respectively. The notion-R_2^-indicates the generated negative triboelectric charge distribution at an r value infinitesimally smaller than R_2; similarly R_2^+denotes the generated positive triboelectric charge distribution at an r value infinitesimally larger than R_2. Since the electric potentials of the two electrodes are equal to each other at SC conditions, ϕ_1 (R_1, 0, z, t) = ϕ_2 (R_3, 0, z, t), and the transferred charges σ_U and SC current (I_{SC}) can then be obtained (Note S2, Supporting Information). According to Eqs. (6) and (7), the radial and axial components of electric fields can be derived. Through Eq. (3), the displacement current through the cylindrical surface r at SC condition is ($I_{D,r}$) given by (Note S2, Supporting Information):

$$\begin{aligned}
I_{D,r} &= \int_S \frac{\partial \boldsymbol{D}}{\partial t}\cdot\boldsymbol{n}\,dS \\
&= +\frac{\sigma_T R_{2^-}}{4\pi}\frac{\partial}{\partial t}\left\{\int_0^{2\pi}\int_{-\infty}^{+\infty} r d\varphi dz\int_0^{2\pi}\right. \\
&\quad\left.\times\int_L^{L+a(t)}\frac{r-R_{2^-}\cos\theta}{\left[R_{2^-}^2+r^2-2rR_{2^-}\cos\theta+(z-z')^2\right]^{\frac{3}{2}}}d\theta dz'\right\} \\
&-\frac{\sigma_T R_{2^+}}{4\pi}\frac{\partial}{\partial t}\left\{\int_0^{2\pi}\int_{-\infty}^{+\infty} r d\varphi dz\int_0^{2\pi}\right. \\
&\quad\left.\times\int_0^{a(t)}\frac{r-R_{2^+}\cos\theta}{\left[R_{2^+}^2+r^2-2rR_{2^+}\cos\theta+(z-z')^2\right]^{\frac{3}{2}}}d\theta dz'\right\} \\
&+\frac{R_1}{4\pi}\frac{\partial}{\partial t}\left\{\sigma_{E1}\int_0^{2\pi}\int_{-\infty}^{+\infty} r d\varphi dz\int_0^{2\pi}\right. \\
&\quad\left.\times\int_{a(t)}^{L}\frac{r-R_1\cos\theta}{\left[R_1^2+r^2-2rR_1\cos\theta+(z-z')^2\right]^{\frac{3}{2}}}d\theta dz'\right\} \\
&-\frac{\sigma_{T1} R_1}{4\pi}\frac{\partial}{\partial t}\left\{\int_0^{2\pi}\int_{-\infty}^{+\infty} r d\varphi dz\int_0^{2\pi}\right. \\
&\quad\left.\times\int_L^{L+a(t)}\frac{r-R_1\cos\theta}{\left[R_1^2+r^2-2rR_1\cos\theta+(z-z')^2\right]^{\frac{3}{2}}}d\theta dz'\right\} \\
&+\frac{\sigma_{T3} R_3}{4\pi}\frac{\partial}{\partial t}\left\{\int_0^{2\pi}\int_{-\infty}^{+\infty} r d\varphi dz\int_0^{2\pi}\right. \\
&\quad\left.\times\int_0^{a(t)}\frac{r-R_3\cos\theta}{\left[R_3^2+r^2-2rR_3\cos\theta+(z-z')^2\right]^{\frac{3}{2}}}d\theta dz'\right\} \\
&-\frac{R_3}{4\pi}\frac{\partial}{\partial t}\left\{\sigma_{E3}\int_0^{2\pi}\int_{-\infty}^{+\infty} r d\varphi dz\int_0^{2\pi}\right. \\
&\quad\left.\times\int_{a(t)}^{L}\frac{r-R_3\cos\theta}{\left[R_3^2+r^2-2rR_3\cos\theta+(z-z')^2\right]^{\frac{3}{2}}}d\theta dz'\right\} \\
&+\frac{R_3}{4\pi}\frac{\partial}{\partial t}\left\{\sigma_{U3}\int_0^{2\pi}\int_{-\infty}^{+\infty} r d\varphi dz\int_0^{2\pi}\right. \\
&\quad\left.\times\int_{a(t)}^{L}\frac{r-R_3\cos\theta}{\left[R_3^2+r^2-2rR_3\cos\theta+(z-z')^2\right]^{\frac{3}{2}}}d\theta dz'\right\} \\
&-\frac{R_1}{4\pi}\frac{\partial}{\partial t}\left\{\sigma_{U1}\int_0^{2\pi}\int_{-\infty}^{+\infty} r d\varphi dz\int_0^{2\pi}\right. \\
&\quad\left.\times\int_{a(t)}^{L}\frac{r-R_1\cos\theta}{\left[R_1^2+r^2-2rR_1\cos\theta+(z-z')^2\right]^{\frac{3}{2}}}d\theta dz'\right\}
\end{aligned} \tag{9}$$

Using this equation, a comparison between the dynamic changes of displacement current and conduction current explains why the displacement current is the driving force of TENGs. Similarly, the open-

circuit voltage (V_{OC}) is derived in Note S2, Supporting Information. If connecting a resistor Z_L between the two electrodes, based on Eq. (4) the potential difference across the external load is

$$-Z_L A\frac{d\sigma_U}{dt} = \Phi_1(R_1, 0, z, t) - \Phi_2(R_3, 0, z, t) \tag{10}$$

Here, ϕ_1 (R_1, 0, z, t) and ϕ_2 (R_3, 0, z, t) represent the electric potential of the two electrodes, respectively; A is the normal contacting area of the cylindrical LS mode TENG. Solving the first-order linearly differential equation, we can determine the temporal dependence of the transferred charges, conduction current, voltage, and power, which allow us to obtain the time-varying electric field, polarization, displacement current and quasi-electrostatic energy and so on; eventually predicting the dynamic output characteristics of the cylindrical LS mode TENG.

2.3. Capacitive modeling of the cylindrical LS mode TENG

The prevailing capacitive model of a TENG device is established based on an infinitely large parallel-plate configuration. A drawback of this model is that it is incapable of revealing the variation of field quantities of TENG device, such as the time-varying electric field, electric displacement, due to the assumption of infinite evenly charged surfaces. Yet, when the relative moving distance is small or/and the edge effect can be neglected [30], this capacitive model is accurate, simple, and easily comprehensible. Accordingly, it is exceedingly feasible to identify the transferred charge, current, voltage, or other circuit variables in the external circuit.

Owing to the lumped-parameter equivalent circuit theory, the equivalent circuit model of a TENG is represented by a capacitor (C_T) and connected in series to an ideal voltage source (V_{OC}). The total capacitance C and V_{OC} of the cylindrical LS mode TENG are (Note S3, Supporting Information)

$$C = \frac{1}{d_0}2\pi\varepsilon_0(L - a(t)) \tag{11}$$

$$V_{OC} = \int_{R_1}^{R_2} E_{r1}dr_1 + \int_{R_2}^{R_3} E_{r2}dr_2 = \frac{\sigma_T R_2 d_0 a(t)}{\varepsilon_0(L - a(t))} \tag{12}$$

Here, the dimension-less parameter $d_0 = \ln(R_2/R_1)/\varepsilon_{r1} + \ln(R_3/R_2)/\varepsilon_{r2}$ represents the effective thickness of the dielectric media; E_{r1} and E_{r2} are the electric field inside the inner dielectric and outer dielectric, respectively. Based on Ohm's law and Kirchhoff's voltage law, the governing equation of the capacitive model is written as (Note S3, Supporting Information)

$$Z_L\frac{dQ(t)}{dt} = V(t) = -\frac{1}{C(t)}Q(t) + V_{OC}(t) = -\frac{d_0 Q(t)}{2\pi\varepsilon_0(L - a(t))} + \frac{\sigma_T R_2 d_0 a(t)}{\varepsilon_0(L - a(t))} \tag{13}$$

As mentioned before, this equation is a first-order ordinary differential equation. Solving this equation, we can obtain the basic output performances of the TENG energy harvesting system.

2.4. Output characteristics of the cylindrical LS mode TENG

Numerical experiments have been carried out to verify the validity of the derived expressions. It should be noticed that the edge effect, which is the non-uniform electric field distribution at the edge of the charged surface, is inevitable for a TENG device according to the theory of electrostatics. To lower the impact of edge effects the largest relative distance is fixed at 0.9 L in this work. The electric potential of the inner electrode is positive while that of the external electrode is negative at OC conditions (Fig. 1c). When the triboelectric charges are created on the contacting surfaces (as an example, $+\sigma_T$ on the external surface of the inner dielectric), the generation of an electric field results in polarization of the dielectric material. The polarization is shielded by induced charges of opposite sign at the interface of the dielectric-electrode (σ_{T1} and σ_{T3}) on the non-overlapping region. In the overlapping region, the caused induced charges ($+\sigma_{E1}$ and $-\sigma_{E3}$) have the same sign as the triboelectric charges since the total charge on each electrode is zero at OC conditions (Fig. 1d). That is why the direction of the radial electric field (E_r) penetrating through the overlapping region is just the opposite compared to that at the non-overlapping region (from "A" to "B" and "C" to "D") (Fig. 1e). Moreover, the real charge distribution on the surface of each electrode depends on the geometry structure of the electrode. According to the theory of electrostatics, the electric field on a conducting surface is normal to the surface everywhere. And the surface of the conductor is an equipotential surface at static/quasi-static conditions. In other words, charges must redistribute to reach electrostatic equilibrium. Therefore, the electric potential at any point on the electrode can be utilized to indicate the electric potential applied to the inner/external electrode; however, this approach is inapplicable to obtain the total electric field generated by charge distributions.

Although the magnitude of E_r within dielectric 1 is smaller than that propagating through dielectric 2 (Fig. 2a), the radial component polarization (P_r) of the former is stronger than the latter, due to the larger relative permittivity of dielectric 1 (ε_{r1}). Since there are no free charges at the interface of the overlapping region, the radial component electric displacement (D_r) is continuous across the contact surfaces (Fig. S2b). The magnitude of E_r increases as the moving distance (z) increases (Fig. 2b) since induced charges are distributed on the non-overlapping regions to ensure the total charge is zero on the electrode. The calculations from the mathematical model agree well with the simulations of FEM, indicating the validity and accuracy of the cylindrical LS mode TENG. A similar tendency for the electric potential is revealed in Fig. 2c. V_{OC} calculated three different ways are exactly identical at small z values but a deviation occurs when z is close to the length of the dielectric (Fig. 2d). The reason for this behavior is attributed to the non-uniform distribution of electric field. To maintain the electrode electrically neutral, a multitude of induced charges is accumulated at the small overlapping region resulting in a strong distortion of edge electric field, which cannot be neglected. However, the latter edge effect is not included in the capacitive model. This is the reason behind deviations between the capacitive model and more detailed FEM simulations.

Subject to SC conditions, charges are transferred between the two electrodes to maintain electrostatic equilibrium. And no charges are distributed in the overlapping region, i.e., σ_E is equal to zero, a result which is significantly different compared to OC conditions. The variation in D_r across dielectric 2 at $z = 0.45\ L$ versus time and relative distance directly reflects the charge distributions (Figs. 3a, S2a and S2b). Also note that the magnitude of D_r is zero at the overlapping region, while it is close to 10 μC/m^2 at the non-overlapping area (Figs. 3b and S2c) at the three points ($z = 0.2\ L$, 0.5 L, 0.8 L) on the inner surface of the outer electrode, demonstrating that only part of the dielectric is polarized during TENG operation.

Owing to the dielectric polarization, quasi-electrostatic energy (W) is generated and distributed in the TENG structure which can be numerically calculated using the approach in Ref. [13,26]. Results shown in Fig. 3c indicate the quasi-electrostatic energy-time relationship of the cylindrical LS mode TNEG under SC conditions, where W_{die1}, W_{die2} and W_{total} represent the energy in the inner dielectric, external dielectric and the total energy, respectively. Notice that the quasi-electrostatic energy is proportional to the moving distance z (Fig. 3c), which is a result of transferred charges through the external circuit as z increases. In addition, a slightly bigger Q_{SC} value is obtained from the mathematical model as a result of a larger calculated capacitance of TENG device (Figs. 3d and S2d). Furthermore, a comparison of conduction and displacement currents depicted in Fig. 3e implies that they are of the same magnitude but opposite in phase.The relationship between them is attributed to the change of the electric flux passing through the Gaussian surface and the change of the total charges distributed in it. In particular, the peak of the displacement current ($I_{D,SC}$) is proportional to the

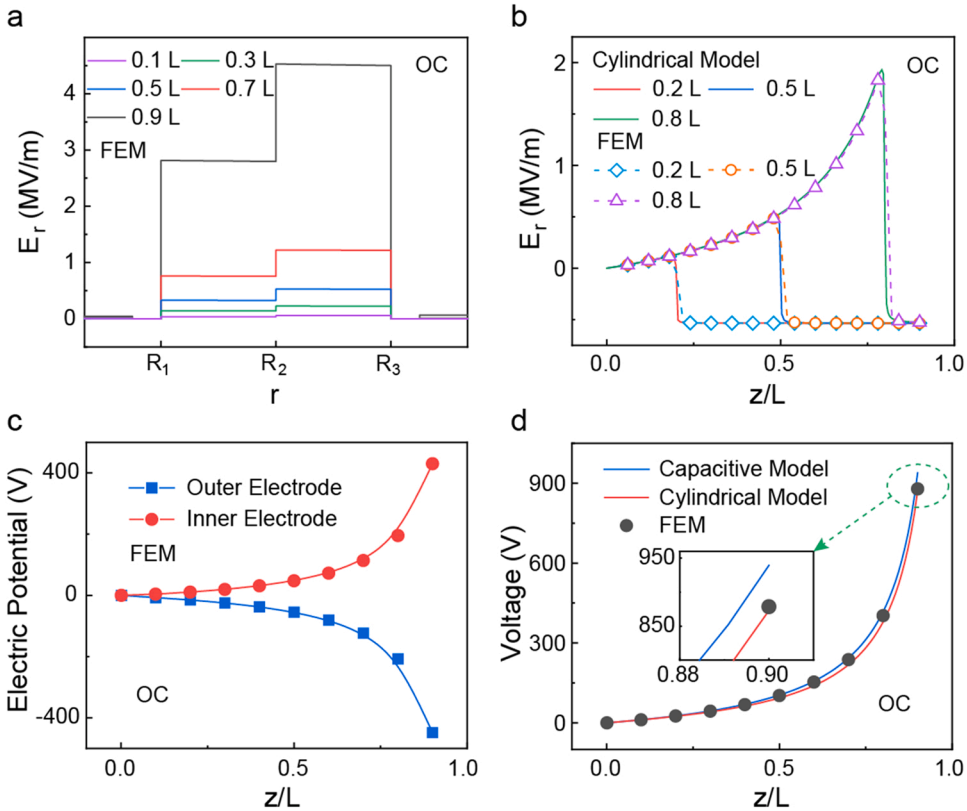

Fig. 2. FEM simulations, cylindrical model and capacitive model results of the cylindrical LS mode TENG at open-circuit (OC) condition. (a) The radial component of the electric field (E_r) distribution at different movement distances from FEM simulations. (b) Comparison of E_r at three fixed points ($r = R_3$, $z = 0.2\ L$, $0.5\ L$, and $0.8\ L$) from FEM simulations and cylindrical model. (c) Electric potentials of the two electrodes from FEM simulations at different relative moving distances z. (d) Comparison of V_{OC} from FEM simulation, cylindrical model and capacitive model. Detailed parameters of these calculations are shown in Table S1.

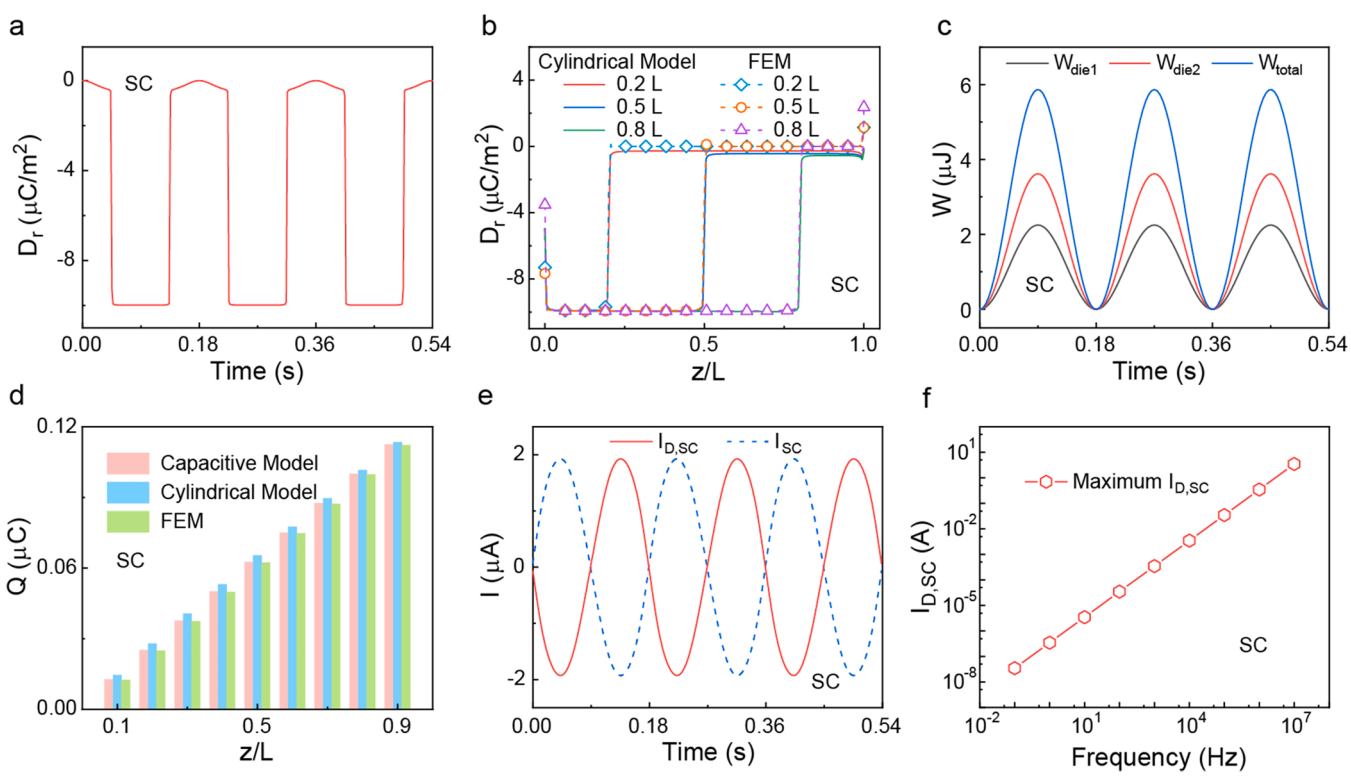

Fig. 3. FEM simulations, cylindrical model and capacitive model results of the cylindrical LS mode TENG under short-circuit (SC) condition. (a) Variation of radial component of the electric displacement (D_r) inside the external dielectric 2 versus time at $z = 0.45\ L$. (b) Comparison of D_r at three fixed points ($r = R_3$, $z = 0.2\ L$, $0.5\ L$, and $0.8\ L$) inside external dielectric media 2 from FEM simulations and cylindrical model. (c) Variations of the qusi-electrostatic energy (W) inside dielectric media 1 (W_{die1}), dielectric media 2 (W_{die2}) and the sum of them (W_{total}) versus time. (d) Comparison of transferred charges (Q) at different relative moving distance z from FEM simulations, cylindrical model and capacitive model. (e) Variations of the displacement current ($I_{D,SC}$) and conduction current (I_{SC}) versus time from cylindrical model at SC condition. (f) Relationship between the peak of I_D and mechanical frequency.

mechanical frequency as expected.

The charge distributions under external loading conditions are similar to those at SC conditions. Since most mechanical energy harvesting systems based on TENG operation are non-linear time-invariant systems, three representative input waveforms: sinusoidal excitation, square excitation and sawtooth excitation have been analyzed. We notice that a square signal yields the highest output among the three signal types followed by sinusoidal and sawtooth signals (in that order) for the same input frequency and amplitude (Figs. 4a, b, and S3). Although the power output behavior of TENGs depend sensitively on the mechanical input conditions, we take the sinusoidal excitation as an example to reveal the TENG's output efficiency. Again, keeping in mind that any waveform can be decomposed into a superposition of sine waves with different frequencies. The largest closed area of the *V-Q* curve in Fig. 4c is a measure of the largest transformed energy; in particular if the load is taken as the optimum load. The *Q-t*, *V-t*, *I-t* and *P-t* curves from Fig. S4 depict how the basic outputs change with external load resistances. Alternatively, the optimum resistance of a TENG device can be obtained from the maximum power transfer theorem. As demonstrated in Fig. 4d, there are three different optimum loads for the three mechanical frequencies. As the mechanical frequency increases, the corresponding optimum resistance decreases, resulting in an increased average power. However, this does not mean we can increase the external frequency to infinity, because operation in practice is restricted by complex conditions such as stability and strength of the TENG geometry structure [31,32].

Effective values are important to evaluate the effectiveness of a voltage or current in delivering power to a resistive load. Here the effective values are calculated by the root-mean-square (*rms*) method [13,14,33]. Our results confirm again that the average power is equivalent to the product of *rms* voltage (V_{rms}) and *rms* current (I_{rms}) (Fig. 4e) [13,14]. More significantly, we further demonstrate that the V_{rms} and *rms* transferred charges (Q_{rms}) under optimum load do not change as the external frequency increases/decreases which has never been reported before (Fig. 4f). However, if any of the external resistances is loaded (for instance, 1×10^8 Ω in Fig. S5a), increasing the working frequency (from 1 Hz to 10 Hz) means decreasing the internal impedance of TENGs. In essence, this is identical to connecting a larger load resistance in the external circuit whereby more potentially usable energy is wasted due to impedance mismatch. On the other hand, the V_{rms}, Q_{rms} and I_{rms} keeps increasing or decreasing as the external resistance increases at a fixed frequency (Fig. S5). A complete understanding of the influence of the above phenomena for energy harvesting is still missing.

Physically, a larger external load reduces the charge transfer rate between the two electrodes but increases the transition time. As a result, more time is needed to reach steady-state. Increasing the external

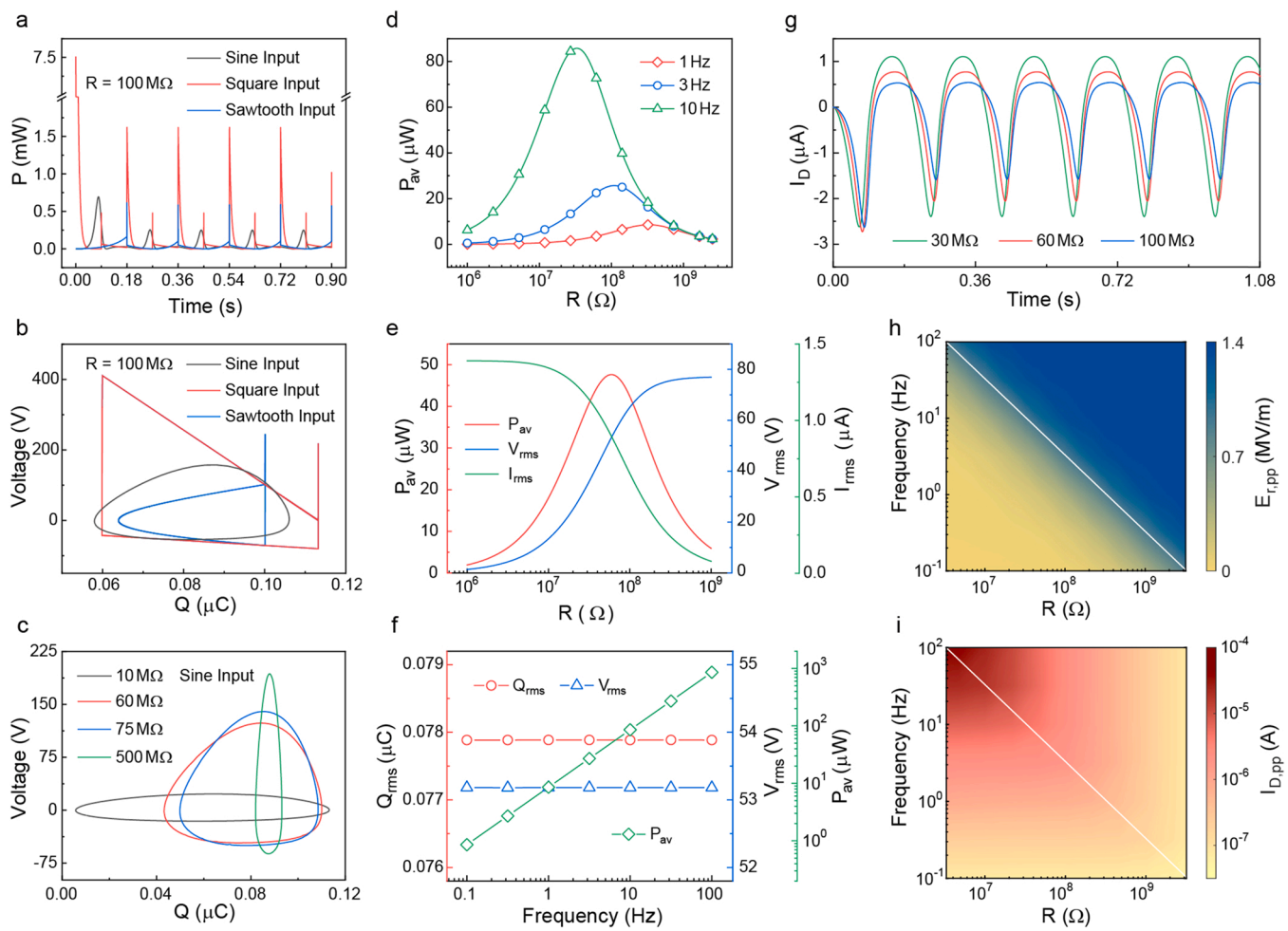

Fig. 4. Output characteristics of the cylindrical LS mode TENG at different excitation conditions. (a) Variations of power versus time and (b) *V-Q* curves at $R = 100$ MΩ for three different input waveforms. (c) *V-Q* curves under four different loads ($R = 10$ MΩ, 60 MΩ, 75 MΩ, and 500 MΩ) for sine input wave. (d) The influence of load resistance on average power (P_{av}) for three different frequencies (1 Hz, 3 Hz and 10 Hz) and on (e) root-mean-square voltage (V_{rms}) and root-mean-square current (I_{rms}). (f) Variations of root-mean-square transferred charge (Q_{rms}), V_{rms} and P_{av} versus frequency under optimum resistance. (g) Variations of I_D versus time for three different loads ($R = 30$ MΩ, 60 MΩ and 100 MΩ). (h) The map of the peak-peak of E_r ($E_{r,pp}$), and (i) the peak-peak of I_D ($I_{D,pp}$) under different load resistances and frequencies.

frequency means decreasing the internal impedance of TENG device which reduces the external optimum load resistance accordingly. At a small mechanical frequency, a larger optimum load resistance is required to match the internal impedance of TENG device; finally, only a small amount of charges (σ_U) is transferred during relaxation (Fig. S5e). To keep electrostatic equilibrium, charges will be accumulated on the overlapping area of the interface between the dielectric and electrode, finally generating a bigger DC component (Q_{rms}). In addition, the influence of obstructing electron transfer due to the optimum load resistance is nearly identical, which could be the intrinsic reason of generating the similar Q_{rms} and V_{rms} even at different mechanical frequencies (Fig. 4f). It is easy to understand that the average power P_{av} is proportional to the working frequency (Fig. 4f).

A quantitative analysis of the time-varying electric field and polarization is indispensable to determine the variation of the displacement current of a TENG device. Numerical results indicate that the variation of E_r and I_D (as well as P_r) change with opposite phase (Figs. 4g, S7a and b); and both the peak of E_r ($E_{r,peak}$) and peak-peak of E_r ($E_{r,pp}$) gradually increase with the increase of the load resistance but the corresponding peak of I_D ($I_{D,peak}$), and peak-peak of I_D ($I_{D,pp}$) exhibit a reverse trend. This is due to the fact the displacement current I_D is determined by the time derivative of the electric displacement D (Eq. (9)) which is equivalent to the sum of $E_r + P_r$. Or by the definition of Ampere-Maxwell law, the displacement current depends on the rate of change of the electric field with time. At a small load resistance, even close to SC conditions, a large number of charges are transferred between the two electrodes to keep electrostatic equilibrium, which results in a large variation of electric field (and electric displacement), generating lower $E_{r,pp}$ and $E_{r,peak}$ values (Figs. 3 and S7). Instead, higher $E_{r,pp}$ and $E_{r,peak}$ are found for a large loading resistor. Consequently, the trends of $I_{D,pp}$ and $I_{D,peak}$ exhibit an totally opposite character. On the other hand, because of the impact on charge transfer caused by the optimum resistor, the $E_{r,pp}$ and $E_{r,peak}$ do not change with the mechanical frequency (Figs. 4i and S7); but $I_{D,pp}$ and $I_{D,peak}$ are proportional to these frequencies (Figs. 4, and S7), illustrating a similar trend as the changing of I_{rms} demonstrated in Fig. S5d.

2.5. Output efficiency

As a new energy conversion technology, a TENG device converts mechanical energy into electricity. From this aspect its operation is different from a traditional capacitor. During the energy conversion process, part of the transformed energy is distributed in the TENG device as a form of quasi-electrostatic energy, and the other part is extracted by the resistor in the external circuit. Since it is not appropriate to utilize the general definition of energy conversion efficiency for the TENG energy harvesting system [34,35], here the output efficiency (η_{output}) of the cylindrical LS mode TENG is calculated by the equation: $\eta_{output} = \frac{E_{load}}{E_{die,av}+E_{load}}$, where E_{load} and $E_{die,av}$ represent the electric energy delivered to the external load and the average quasi-electrostatic energy stored in TENG device during the steady state, respectively.

The largest η_{output} of the cylindrical LS mode TENG, which is close to 70% obtained at an optimum resistance for a fixed excitation frequency (Fig. 5a and b). As such, this demonstrates that nearly 70% electrical energy is extracted into the external circuit, but the remainder electricity is unavailable during the TENG operation. Loading a small or a large resistor can cause impedance mismatch, which leads to substantial waste in the energy transfer process and a decrease in the output efficiency. On one hand, if a small load is connected, the electrical energy extracted into the external circuit is faster than that stored in the TENG. When a large resistor is loaded, the reverse trend takes place (Fig. 5a and b). On the other hand, the largest η_{output} is obtained at the optimum resistor at different mechanical frequencies (Fig. 5a and c). The new findings may inspire researchers to reconsider the relationship between the maximum energy output efficiency and power management circuit.

3. Conclusion

Combining the expanded Maxwell's equations and the geometric configuration, a new model for the cylindrical lateral sliding mode TENG is proposed for thoroughly revealing the time-varying electric field and electric potential as well as the basic output characteristic of TENGs. Finite Element Method (FEM) simulations and semi-analytical analysis validate the variations of electric field, polarization, electric displacement, and electric potential subject to different boundary conditions. The dynamics of the displacement current is shown to be the driving force of TENGs. Studies of three typical mechanical excitations indicate that the largest output is obtained for a square-wave input signal. Importantly, at an optimum load resistance the effective values of transferred charges, voltage, and the highest output efficiency (close to 70%) nearly stay the same as the mechanical frequency increases. It must be noticed that these findings require significant attention; yet, they have not been reported before in the literature. We have confirmed great potential in extending a detailed theoretical model to other more complex geometric configurations such as the non-planar charge distribution, allowing us to demonstrate quantitatively the variation of

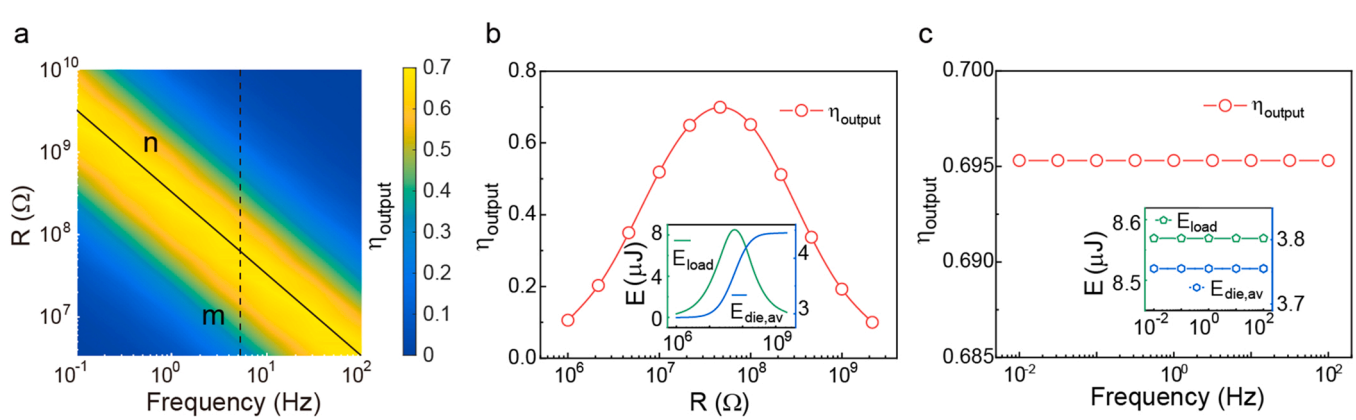

Fig. 5. The output efficiency (η_{output}) of the cylindrical LS mode TENG at different frequencies and loading conditions. (a) The map of η_{output} at different load resistances and frequencies. (b) Variation of η_{output} under different loading conditions. The inset demonstrates the change of the transferred energy. E_{load}, and $E_{die,av}$ represent the extracted electric energy and the average quasi-electrostatic energy stored in TENG device, respectively. (c) Variation of η_{output} at different frequencies under optimum resistance.

source and field quantities for different TENG configurations. A comprehensive analysis of the cylindrical mode TENG overcomes the limitations of conventional models constructed from simple charged plane considerations thereby providing a fresh perspective for accurate modeling and prediction of TENG output characteristics subject to complex charge distributions.

4. Methods

The FEM simulations at OC and SC conditions of a cylindrical LS mode TENG were carried out utilizing COMSOL software. Subject to OC boundary conditions, the total surface charges at each electrode are set to 0, while the potentials of the two electrodes are equal to each other under SC boundary conditions. The dynamic output characteristics including the transient output and steady-state output were numerically evaluated by solving the governing equation. After exactly determining the charge distributions in a TENG device, the time-varying electric field, polarization, electric displacement, displacement current, and other field quantities were investigated with detailed numerical simulations. In addition to FEM simulations numerical calculations were performed using MATLAB (Mathworks Inc.). Details and the parameters utilized in computations can be found in the Supporting Information.

CRediT authorship contribution statement

Xin Guo, Jiajia Shao, Zhong Lin Wang: Conceived the idea, inspired the project, Derived analytic expressions, Prepared the manuscript. **Xin Guo, Jiajia Shao**: Constructed the FEM model and simulated numerically using MATLAB and COMSOL Multiphysics software. **Xin Guo, Jiajia Shao, Yi Yang, Morten Willatzen, Zhong Lin Wang**: Discussed the simulation data. **Zhong Lin Wang**: Supervised the project.

Declaration of Competing Interest

The authors declare that they have no known competing financial interests or personal relationships that could have appeared to influence the work reported in this paper.

Acknowledgments

Xin Guo and Jiajia Shao contributed equally to this work. Research supported by the National Key R & D Project from Minister of Science and Technology (Grant No. 2016YFA0202704), National Natural Science Foundation of China (Grant Nos. 62001031, 51702018, and 51432005), Fundamental Research Funds for the Central Universities (Grant No. E0E48957). The authors declare that they have no competing interests. All data needed to evaluate the conclusions in the paper are present in the paper and/or the Supplementary Materials. Additional data related to this paper may be requested from the authors.

Appendix A. Supporting information

Supplementary data associated with this article can be found in the online version at doi:10.1016/j.nanoen.2021.106762.

References

[1] J. Peng, S.D. Kang, G.J. Snyder, Optimization principles and the figure of merit for triboelectric generators, Sci. Adv. 3 (2017), eaap8576.
[2] W.H. Xu, H. Zheng, Y. Liu, X. Zhou, C. Zhang, Y. Song, X. Deng, M. Leung, Z. Yang, R.X. Xu, Z.L. Wang, X.C. Zeng, Z. Wang, A droplet-based electricity generator with high instantaneous power density, Nature 578 (2020) 392–396.
[3] H. Guo, J. Chen, L. Wang, A.C. Wang, Y. Li, C. An, J.H. He, C. Hu, V.K.S. Hsiao, Z. L. Wang, A highly efficient triboelectric negative air ion generator, Nat. Sustain. 4 (2021) 147–153.
[4] X. Peng, K. Dong, C. Ye, Y. Jiang, S. Zhai, R. Cheng, D. Liu, X. Gao, J. Wang, Z. L. Wang, A breathable, biodegradable, antibacterial, and self-powered electronic skin based on all-nanofiber triboelectric nanogenerators, Sci. Adv. 6 (2020), eaba9624.
[5] J. Cheng, W. Ding, Y. Zi, Y. Lu, L. Ji, F. Liu, C. Wu, Z.L. Wang, Nat. Commun. 9 (2018) 3733.
[6] Y. Zi, S. Niu, J. Wang, Z. Wen, W. Tang, Z.L. Wang, Standards and figure-of-merits for quantifying the performance of triboelectric nanogenerators, Nat. Commun. 6 (2015) 8376.
[7] S. Niu, Y. Liu, S. Wang, L. Lin, Y.S. Zhou, Y. Hu, Z.L. Wang, Theory of sliding-mode triboelectric nanogenerators, Adv. Mater. 25 (2013) 6184.
[8] S. Niu, Y.S. Zhou, S. Wang, Y. Liu, L. Lin, Y. Bando, Z.L. Wang, Simulation method for optimizing the performance of an integrated triboelectric nanogenerator energy harvesting system, Nano Energy 8 (2014) 150.
[9] S.M. Niu, S.H. Wang, L. Lin, Y. Liu, Y.S. Zhou, Y.F. Hu, Z.L. Wang, Theoretical study of contact-mode triboelectric nanogenerators as an effective power source, Energ. Environ. Sci. 6 (2013) 3576.
[10] Z.L. Wang, On maxwell's displacement current for energy and sensors: the origin of nanogenerators, Mater. Today 20 (2017) 74.
[11] Z.L. Wang, On the first principle theory of nanogenerators from Maxwell's equations, Nano Energy 68 (2020), 104272.
[12] J.J. Shao, M. Willatzen, T. Jiang, W. Tang, X. Chen, J. Wang, Z.L. Wang, Quantifying the power output and structural figure-of-merits of triboelectric nanogenerators in a charging system starting from the Maxwell's displacement current, Nano Energy 59 (2019) 380–389.
[13] J.J. Shao, M. Willatzen, Z.L. Wang, Theoretical modelling of triboelectric nanogenerators (TENGs), J. Appl. Phys. 128 (2020), 111101.
[14] J.J. Shao, D. Liu, M. Willatzen, Z.L. Wang, Three-dimensional modeling of alternating current triboelectric nanogenerator in the linear sliding mode, Appl. Phys. Rev. 7 (2020), 011405.
[15] R. Hinchet, H.J. Yoon, H. Ryu, M.K. Kim, E.K. Choi, D.S. Kim, S.W. Kim, Transcutaneous ultrasound energy harvesting using capacitive triboelectric technology, Science 365 (2019) 491.
[16] H. Guo, X. Pu, J. Chen, Y. Meng, M.H. Yeh, G. Liu, Q. Tang, B. Chen, D. Liu, Q. Song, C.G. Hu, J. Wang, Z.L. Wang, A highly sensitive, self-powered triboelectric auditory sensor for social robotics and hearing aids, Sci. Robot 3 (2018), eaat2516.
[17] A. Li, Y. Zi, H. Guo, Z.L. Wang, F.M. Fernandez, Triboelectric nanogenerators for sensitive nano-coulomb molecular mass spectrometry, Nat. Nanotechnol. 12 (2017) 481–487.
[18] S. Niu, Z.L. Wang, Theoretical systems of triboelectric nanogenerators, Nano Energy 14 (2015) 161.
[19] J.J. Shao, M. Willatzen, Y. Shi, Z.L. Wang, 3D mathematical model of contact-separation and single-electrode mode triboelectric nanogenerators, Nano Energy 60 (2019) 630.
[20] J.J. Shao, T. Jiang, W. Tang, X. Chen, L. Xu, Z.L. Wang, Structural figure-of-merits of triboelectric nanogenerators at powering loads, Nano Energy 51 (2018) 688.
[21] R.D.I.G. Dharmasena, K.D.G.I. Jayawardena, C.A. Mills, J.H.B. Deane, J.V. Anguita, R.A. Dorey, S.R.P. Silva, Triboelectric nanogenerators: providing a fundamental framework, Energ, Environ. Sci. 10 (2017) 1801.
[22] R.D.I.G. Dharmasena, K.D.G.I. Jayawardena, C.A. Mills, R.A. Dorey, S.R.P. Silva, A unified theoretical model for triboelectric nanogenerators, Nano Energy 48 (2018) 391.
[23] R.D.I.G. Dharmasena, J.H.B. Deane, S.R.P. Silva, Adv. Energy Mat. 8 (2018), 1802190.
[24] Z.L. Wang, T. Jiang, L. Xu, Toward the blue energy dream by triboelectric nanogenerator networks, Nano Energy 39 (2017) 9–23.
[25] L. Huang, S. Lin, Z. Xu, H. Zhou, J. Duan, B. Hu, J. Zhou, Fiber-based energy conversion devices for human-body energy harvesting, Adv. Mater. 32 (2020), 1902034.
[26] J.J. Shao, Y. Yang, O. Yang, J. Wang, M. Willatzen, Z.L. Wang, Designing rules and optimization of triboelectric nanogenerator arrays, Adv. Energy Mater. 11 (2021), 2100065.
[27] J. You, J. Shao, Y. He, F.F. Yun, K.W. See, Z.L. Wang, X. Wang, High-electrification performance and mechanism of a water-solid mode triboelectric nanogenerator, ACS Nano 15 (2021) 8706–8714.
[28] H.T. Baytekin, A.Z. Patashinski, M. Branicki, B. Baytekin, S. Soh, B.A. Grzybowski, The mosaic of surface charge in contact electrification, Science 333 (2011) 308–312.
[29] Z.L. Wang, From contact-electrification to triboelectric nanogenerators, Rep. Prog. Phys. (2021), https://doi.org/10.1088/1361-6633/ac0a50.
[30] J.D. Jackson. Classical Electrodynamics, third ed..,, Wiley & Sons, 1999.
[31] Z. Lin, B. Zhang, H. Zou, Z. Wu, H. Guo, Y. Zhang, J. Yang, Z.L. Wang, Rationally designed rotation triboelectric nanogenerators with much extended lifetime and durability, Nano Energy 68 (2020), 104378.
[32] K. Dong, X. Peng, Z.L. Wang, Fiber/fabric-based piezoelectric and triboelectric nanogenerators for flexible/stretchable and wearable electronics and artificial intelligence, Adv. Mater. 32 (2020) 1902549.

[33] N.J. William. Electric Circuits, third ed..,, Pearson Education, Inc, New Jersey, 2013.
[34] G.Q. Xu, X.Y. Li, X. Xia, J.J. Fu, W.B. Ding, Y.L. Zi, Nano Energy 59 (2019) 154.
[35] J.H.B. Deane, R.D.I.G. Dharmasena, G. Gentile, Power computation for the triboelectric nanogenerator, Nano Energy 54 (2018) 39–49.

Xin Guo received her B.S. degree in the School of Physics at University of Electronic Science and Technology of China in 2020. She is currently pursuing her Ph.D. in Prof. Zhong Lin Wang's group at Beijing Institute of Nanoenergy and Nanosystems, Chinese Academy of Sciences. Her research interests include Maxwell's equations and computational electromagnetics, modeling and simulation of energy harvesting systems.

Jiajia Shao received his Ph.D. degree from University of Chinese Academy of Sciences in 2019, and a postdoctoral fellow at the Beijing Institute of Nanoenergy and Nanosystems, Chinese Academy of Sciences in 2021, under the supervision of Prof. Zhong Lin Wang. Now he is an associate researcher in Prof. Zhong Lin Wang's group. His research interests have been focused on the field of: contact electrification, physical mechanisms of triboelectric nanogenerators, Maxwell's equations and displacement current, modeling & simulation of dynamic physical system.

Dr. Morten Willatzen is a Talent 1000 Foreign Expert and Senior Full Professor at the Beijing Institute of Nanoenergy and Nanosystems, Chinese Academy of Sciences. He also holds a Guest Professor position at the Department of Photonics Engineering, Technical University of Denmark and an Honorary Professorship at the Mads Clausen Institute, University of Southern Denmark. He received his MSc degree from Aarhus University and the PhD degree from the Niels Bohr Institute at the University of Copenhagen. Morten Willatzen's research interests include solid state physics, mathematical physics, piezoelectricity, metamaterials and flow acoustics

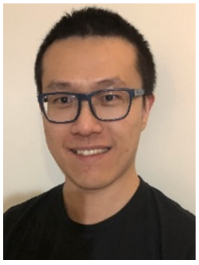

Dr. Yi Yang is a postdoctoral researcher in the Department of Physics and Research Laboratory of Electronics at Massachusetts Institute of Technology (MIT), USA. He received his B.S. and M. S. degrees from Peking University, China and Ph.D. degree from MIT. His current research interests include nanophotonics, plasmonics, free-electron optics, photonic crystals, and topological photonics.

Dr. Zhong Lin Wang is a Hightower Chair and Regents's Professor at Georgia Tech. He is also the Chief scientist and Director for the Beijing Institute of Nanoenergy and Nanosystems, Chinese Academy of Sciences. His discovery and breakthroughs in developing nanogenerators establish the principle and technological road map for harvesting mechanical energy from environmental and biological systems for powering personal electronics. He coined and pioneered the field of piezotronics and piezo-phototronics by introducing piezoelectric potential gated charge transport process in fabricating new electronic and optoelectronic devices.